

# Ru-Doped $\text{Fe}_2\text{TiO}_5$ as a High-Performance Electrocatalyst for Urea-Assisted Water Splitting

Kassa Belay Ibrahim,\* Karim Harrath, Mohammadhossein Hamrang, Matteo Bordin, Stéphanie Bruyère, David Horwat, Enrique Rodríguez-Castellón, Marshet Getaye Sendeku, Pratik Shinde, Danilo Oliveira de Souza, Luca Olivi, Alberto Vomiero,\* Elisa Moretti,\* and Tofik Ahmed Shifa\*

The urea oxidation reaction (UOR), with its low thermodynamic potential, offers a promising alternative to the oxygen evolution reaction (OER) for efficient hydrogen production. However, its sluggish kinetics still demand the development of an efficient electrocatalyst. In this study, the critical role of Ru doping in  $\text{Fe}_2\text{TiO}_5$  is demonstrated to accelerate UOR kinetics. The computational finding confirmed the feasibility of this approach, guiding the experimental synthesis of  $\text{Fe}_{2-x}\text{Ru}_x\text{TiO}_5$ . Benefitting from surface properties and electronic structure, the synthesized material exhibits superior performance with a potential of 1.30 V at a current density of  $10 \text{ mA cm}^{-2}$  for UOR, compared to undoped  $\text{Fe}_2\text{TiO}_5$  (1.40 V). Moreover, it demonstrates a favourable Tafel slope of  $52 \text{ mV dec}^{-1}$  and maintains robust durability for 72 h. As confirmed from experimental and computational findings, the enhanced activity can be attributed to the Ru doping resulting in structural distortion at the Fe site and creation of a favourable adsorption site thereby enhancing UOR via dual active center. This study not only broadens the potential applications of  $\text{Fe}_2\text{TiO}_5$ -based materials beyond their traditional role as photocatalysts but also establishes them as promising electrocatalysts underscoring the versatility and improved performance of  $\text{Fe}_{2-x}\text{Ru}_x\text{TiO}_5$ .

## 1. Introduction

Energy crisis and climate change are the two main challenges encountered recently and have created huge concerns worldwide. Research and development of new renewable energy sources that can replace conventional fossil fuels is of paramount importance.<sup>[1]</sup> Renewable energy generation, that is, hydrogen fuel produced by seawater electrolysis<sup>[2]</sup> through OER<sup>[3]</sup> and HER has emerged as a viable option. Unfortunately, the kinetically sluggish nature of OER, the resulting high overpotential limit (1.23 V), and the high energy consumption required for efficient  $\text{H}_2$  production have significantly impeded the overall performance. Considering the overall water splitting, the OER process requires a high voltage to drive it; therefore, substituting OER with an electro-oxidation reaction with a lower theoretical potential is an efficient methodology to alleviate this

K. B. Ibrahim, M. Hamrang, M. Bordin, P. Shinde, A. Vomiero, E. Moretti, T. A. Shifa

Department of Molecular Sciences and Nanosystems

Ca' Foscari University of Venice

Via Torino 155, Venezia Mestre 30170, Italy

E-mail: [kassabelay.ibrahim@unive.it](mailto:kassabelay.ibrahim@unive.it); [alberto.vomiero@ltu.se](mailto:alberto.vomiero@ltu.se);

[elisa.moretti@unive.it](mailto:elisa.moretti@unive.it); [tofikahmed.shifa@unive.it](mailto:tofikahmed.shifa@unive.it)

K. Harrath

Ganjiang Innovation Academy

Chinese Academy of Science

Ganzhou 341000, P. R. China

S. Bruyère, D. Horwat

Université de Lorraine, CNRS, IJL

Nancy F-54000, France

E. Rodríguez-Castellón

Departamento de Química Inorgánica

Cristalografía y Mineralogía

Facultad de Ciencias

Instituto Interuniversitario de Investigación en Biorrefinerías I3B

Universidad de Málaga

Málaga 29071, Spain

M. G. Sendeku

Ocean Hydrogen Energy R&D Center

Research Institute of Tsinghua University in Shenzhen

Shenzhen 518057, P. R. China

D. O. de Souza, L. Olivi

Elettra-Sincrotrone Trieste

Strada Statale 14, km 163.5, Trieste 34149, Italy

A. Vomiero

Division of Materials Science

Department of Engineering Sciences and Mathematics

Luleå University of Technology

Luleå SE-97187, Sweden

 The ORCID identification number(s) for the author(s) of this article can be found under <https://doi.org/10.1002/smll.202412370>

© 2025 The Author(s). Small published by Wiley-VCH GmbH. This is an open access article under the terms of the [Creative Commons Attribution License](https://creativecommons.org/licenses/by/4.0/), which permits use, distribution and reproduction in any medium, provided the original work is properly cited.

DOI: 10.1002/smll.202412370

issue. Recently, as an alternative to traditional hydrogen production from electrocatalytic water splitting, many readily oxidizable molecules including alcohols,<sup>[4]</sup> glucose,<sup>[5]</sup> urea,<sup>[6,7]</sup> hydrazine,<sup>[8]</sup> and 5-(hydroxymethyl)furfural<sup>[9]</sup> have been deployed to replace the OER process and improve energy efficiency. Owing to the favorable thermodynamics of UOR ( $\text{CO}(\text{NH}_2)_2 + 6\text{OH}^- \rightarrow \text{N}_2 + \text{CO}_2 + 5\text{H}_2\text{O} + 6\text{e}^- = 0.37 \text{ V}$ ) over the OER (1.23 V), this technology can theoretically realize  $\approx 70\%$  of energy saving compared with traditional electrocatalytic water splitting.<sup>[10–14]</sup> Urea plays a significant role in enhancing water-splitting processes, particularly through the UOR, which serves as an alternative to traditional methods for hydrogen production. This approach not only reduces energy consumption but also improves the overall efficiency of hydrogen generation. Therefore, UOR is a thermodynamically favorable process as compared to OER. Furthermore, urea can be considered a “valuable” waste. It is an environmental pollutant released by agricultural fertilizers, industrial processes, and domestic excretion, but it has a high hydrogen content (6.67 wt%).<sup>[15–18]</sup> Moreover, urea is universally available in human urine and industrial and sanitary wastewater, making its electrolysis highly feasible.<sup>[19–23]</sup> However, the practical application of UOR is significantly hindered by major challenges associated with multistep electron transfer ( $6\text{e}^-$  transfer),<sup>[20,24]</sup> including slow kinetics, complex intermediate adsorption/desorption, and high overpotential. By exploiting UOR, we could utilize its potential as an energy carrier and mitigate its environmental impact. Until now, the state-of-the-art catalysts for urea electrolysis are noble metals, whereas their prohibitive cost, scarce reserves, and poor stability hinder widespread application. So, developing efficient, cheap, and robust UOR catalysts is highly urgent.

Recently it has been reported that several synthesis approaches and material design strategies are suitable for producing highly efficient UOR catalysts. The optimization of advanced catalyst performance involves various aspects such as porosity development, heterostructure design, defect engineering, surface functionalization, electronic structure modulation, and overall modifications of their structural and chemical properties.<sup>[25]</sup> Moreover, nowadays there is a strong emphasis on researching nonprecious transition metal-based catalysts, particularly Ni, Co, Mn, and Fe-based catalysts, which show promising performance in UOR and OER.<sup>[11,26,27]</sup> Catalysts such as  $\text{CoSe}_2/\text{NiSe}_2$ ,<sup>[28]</sup>  $\text{Ni}(\text{OH})_2$ ,<sup>[29]</sup>  $\text{Ni}(\text{OH})_2/\text{SnS}_2$ ,<sup>[30]</sup>  $\text{MoS}_2/\text{Ni}_3\text{S}_2$ ,<sup>[31]</sup> Ti-doped  $\text{Fe}_2\text{O}_3$ ,<sup>[32]</sup> have been widely studied and have demonstrated excellent properties.<sup>[20,33–36]</sup>

Iron-based catalysts hold great potential due to their earth-abundance and low toxicity.<sup>[16]</sup> Yet, the poor electronic conductor nature of iron-based catalysts results in the formation of Schottky barriers between the catalyst and the electrolyte, as well as between the catalyst and the current collector, leading to sub-optimal catalytic activity in these compounds.<sup>[37,38]</sup> These limitations can be addressed through elemental doping, which is a universal strategy to engineer the electronic and chemical properties of materials. This approach modifies the electronic structure of catalysts, creating new surface active sites and expediting the charge transfer.<sup>[39]</sup> Various studies have suggested that pseudobrookite  $\text{Fe}_2\text{TiO}_5$  can be used as light-harvesting materials in PEC devices and as surface coatings to provide corrosion resistance.

In this work, we introduce a new active site with strong interaction with O to construct the dual active centers which may be an effective strategy to break adsorption-energy scaling limitations, and thus improve the UOR activity.<sup>[40–42]</sup> The  $\text{Ru}^{4+}$  with the electronic configuration of  $[\text{Kr}]4d$  has been reported to be a suitable adsorption site of  $\text{H}_2\text{O}$ , OH, and  $\text{N}_2$  to participate in alkaline UOR and OER.<sup>[43]</sup>

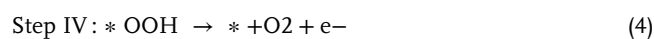
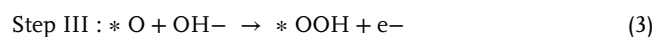
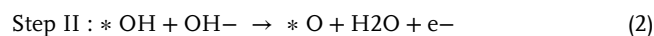
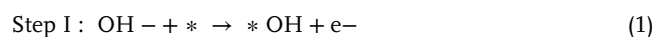
Herein, we successfully introduce Ru dopants in  $\text{Fe}_2\text{TiO}_5$ , via a hydrothermal and CVD process for electrocatalytic hydrogen production via water and urea electrolysis. The obtained product exhibited superior activities and long-term durability toward UOR and OER. When used as a UOR and OER electrocatalyst, low electrode potentials of 1.30 V and 1.40 V could be achieved to reach a current density of  $10 \text{ mA cm}^{-2}$  in 1.0 M KOH aqueous solutions with the absence and presence of 0.5 M urea, respectively. Also, density functional theory (DFT) simulations confirm that the charge distribution from Ru to  $\text{Fe}_2\text{TiO}_5$  at the heterojunction's interfaces is advantageous for decomposing  $\text{CO}(\text{NH}_2)_2$  and optimizing and accelerating UOR and OER.<sup>[7]</sup>

## 2. Experimental Section

### 2.1. Theoretical Simulations

To gain an understanding of the effect of Ru doping on the performance of the pristine  $\text{Fe}_2\text{TiO}_5$  catalyst, first, the most stable phase was computationally studied when Ru substitutes Ti atoms on the surface, forming  $\text{Fe}_2\text{Ru}_x\text{Ti}_{1-x}\text{O}_5$ , or substitutes Fe atoms, forming  $\text{Fe}_{2-x}\text{Ru}_x\text{TiO}_5$ . To understand this phenomenon, Spin-polarized DFT+U calculations were performed using the revised Perdew-Burke-Ernzerh of (RPBE) exchange-correlation functional<sup>[44]</sup> within the Vienna Ab Initio Simulation Package (VASP).<sup>[45]</sup> The projector-augmented wave (PAW) method<sup>[46,47]</sup> with a plane-wave kinetic energy cutoff of 500 eV was utilized, along with Gaussian smearing of 0.05 eV. The DFT+U correction was applied with U values of 3 eV for Fe and 3.2 eV for Ti.<sup>[48,49]</sup> The Brillouin zone was sampled using a  $3 \times 3 \times 1$  k-point mesh for geometry optimization and a  $6 \times 6 \times 1$  k-point mesh for projected density of states (PDOS) calculations. The  $\text{Fe}_2\text{TiO}_5$  (101) surface was modeled using a  $(3 \times 3)$  supercell with a 15 Å vacuum layer to prevent periodic interactions. The Ru-doped  $\text{Fe}_2\text{TiO}_5$  was modeled as shown in **Figure 1a–c**. All atoms were relaxed during geometry optimization until the forces were less than 0.03 eV/Å. The isolated molecules ( $\text{O}_2$ ,  $\text{H}_2$ ,  $\text{H}_2\text{O}$ ,  $\text{N}_2$ ,  $\text{CO}_2$ , and  $\text{CO}(\text{NH}_2)_2$ ) were optimized within a unit cell of  $15 \text{ Å} \times 15 \text{ Å} \times 15 \text{ Å}$  using only the  $\Gamma$ -point.<sup>[50]</sup> Van der Waals corrections were incorporated using Grimme's method with Becke–Johnson damping.<sup>[51]</sup>

The oxygen evolution reaction (OER) performance of  $\text{Fe}_2\text{TiO}_5(101)$  and Ru-doped models was predicted using Gibbs free-energy ( $\Delta G$ ) profiles for the following elementary OER steps, according to Norskov et al.:<sup>[52]</sup>



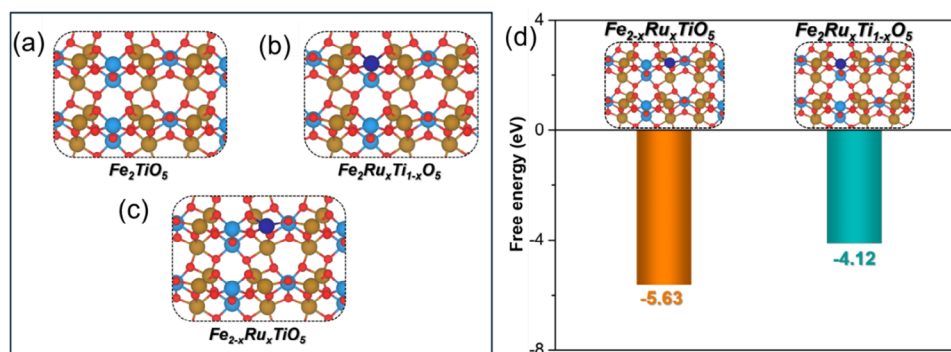
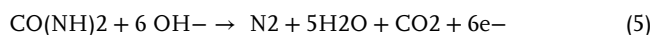


**Figure 1.** Catalyst surface models are investigated in this work. a)  $\text{Fe}_2\text{TiO}_5$ , b)  $\text{Fe}_2\text{RuxTi}_{1-x}\text{O}_5$ , c)  $\text{Fe}_{2-x}\text{RuxTiO}_5$ . d) Formation energy of  $\text{Fe}_2\text{RuxTi}_{1-x}\text{O}_5$  and  $\text{Fe}_{2-x}\text{RuxTiO}_5$  from  $\text{Fe}_2\text{TiO}_5$ .

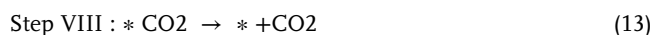
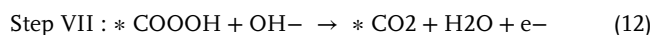
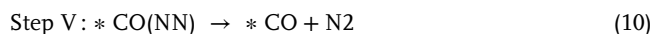
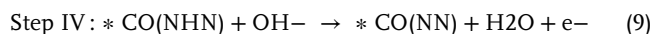
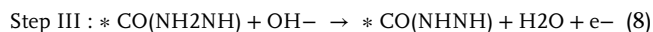
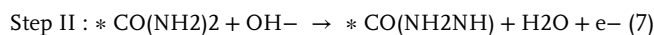
where \* represents the bare site and \*OH, \*O, \*O<sub>2</sub>, and \*OOH denote the surface featuring different chemisorbed species. The free energy difference for all of the above elementary steps ( $\Delta\text{GOH}^*$ ,  $\Delta\text{GO}^*$ ,  $\Delta\text{GOOH}^*$ ) involving an electron transfer is calculated by the equation  $\Delta G = \Delta E + \Delta\text{ZPE} - T\Delta S + \Delta G U + \Delta G \text{pH}$ , where  $\Delta E$ ,  $\Delta\text{ZPE}$ , and  $\Delta S$  correspond to the energy difference between adsorption energy, zero-point energy, and entropy, respectively. The adsorption energies  $\Delta E$  were measured using DFT. The  $\Delta\text{ZPE}$  and  $T\Delta S$  values were obtained from vibrational frequency calculations and DFT.  $\Delta G U = -eU$ , where  $U$  represents a potential based on a standard hydrogen electrode.  $\Delta G \text{pH}$  describes the Gibbs free energy correction of the pH, noting that it considers pH 12.

Under ideal conditions, the OER reaction with a total energy change of 4.92 eV can be driven at 1.23 V. In comparison, the free energy of each elementary reaction would be equally divided into 1.23 eV. Thus, the overpotential  $\eta$  is introduced to represent the additional required potential and to rationalize the catalytic performance of the catalyst, which is defined in theoretical calculations as:  $\eta = \max(\Delta G_{(1,2,3,4)})/e - 1.23 \text{ eV}$ .

The overall reaction equation of urea oxidation (UOR) is presented as follows:



where the specific elementary steps are considered according to the following scheme:



## 2.2. Synthesis of the Electrocatalyst

### 2.2.1. Materials

These reagents were used without further purification: iron(III) nitrate nonahydrate ( $\text{Fe}(\text{NO}_3)_3$ , Merck  $\geq 99.95\%$ ), isopropanol ( $(\text{CH}_3)_2\text{CHOH}$ , Merck  $\geq 99.5\%$ ), titanium(IV) isopropoxide ( $\text{Ti}(\text{OCH}(\text{CH}_3)_2)_4$ , Merck %97), ruthenium(III) chloride nonahydrate ( $\text{RuCl}_3 \cdot 9\text{H}_2\text{O}$ , Merck 45–55%), absolute ethanol ( $\text{CH}_3\text{CH}_2\text{OH}$ ), deionized water ( $\text{H}_2\text{O}$ ).

**Synthesis of pseudobrookite  $\text{Fe}_2\text{TiO}_5$ :** To synthesize the pseudobrookite  $\text{Fe}_2\text{TiO}_5$ , 2.51 mmol of  $\text{Fe}(\text{NO}_3)_3 \cdot 9\text{H}_2\text{O}$  were dissolved in 50 mL of isopropanol under stirring. Then, 1.25 mmol of  $\text{Ti}(\text{OCH}(\text{CH}_3)_2)_4$  were added dropwise to the solution. The resulting mixture underwent stirring for 1 hr. Then, the solution was transferred to a Teflon-lined stainless-steel autoclave and subjected to a solvothermal treatment at 150 °C for 12 hrs, with a controlled heating rate of 10 °C  $\text{min}^{-1}$ . After cooling, the suspension was centrifuged and washed with deionized water and isopropanol three times. The powder was then dried in a 60 °C oven for 12 h, then calcinated in a furnace at 800 °C for 3 h.

**Synthesis of  $\text{Fe}_{2-x}\text{RuxTiO}_5$ :** In a typical process of  $\text{Fe}_{2-x}\text{RuxTiO}_5$  synthesis (Scheme S1), 5.01 mmol  $\text{Fe}_2\text{TiO}_5$ , and 0.1082 mmol  $\text{RuCl}_3 \cdot 9\text{H}_2\text{O}$  were dissolved in 10 mL of ethanol under stirring for 3 hrs. Later, 20 ml of deionized water were added to the solution and stirred for 3 h. The entire solution was then transferred to a Teflon-lined stainless-steel autoclave and subjected to a thermal treatment at 150 °C for 12 h. After natural cooling, the resulting sample was centrifuged and dried for 12 h at 60 °C, followed by calcination at 300 °C for 2 h under Ar atmosphere.

### 2.3. Material Characterization Techniques

The samples' crystalline structure and phase composition were examined using X-ray diffraction (XRD) on a TZY-XRD (D/MAX-TTRIII(CBO)) system with Cu-K $\alpha$  radiation ( $\lambda = 1.5418 \text{ \AA}$ ). The morphology and microstructure were characterized through Scanning Electron Microscopy (SEM) on a Hitachi S4800 field-emission scanning electron microanalyzer coupled with energy-dispersive X-ray spectroscopy (EDX). High-resolution Transmission Electron Microscopy (HR-TEM) and High Angle Annular Dark Field – Scanning Transmission Electron Microscopy

(HAADF-STEM) micrographs were also recorded via Nancy JEOL ARM 200F with 2 CS correctors. The TEM has an in Nancy: MSC794 camera Gatan one view, JEOL HAADF detector, and a double-tilt sample holder. X-ray photoelectron spectroscopy (XPS) measurements were carried out in a PHI 5700 Physical Electronics spectrometer, with non-monochromatic Mg K $\alpha$  radiation equipped with a multichannel detector. X-ray absorption spectroscopy (XAS) measurement at Fe K-edge was carried out at the XAFS experimental end station of the synchrotron Elettra (Andrea Di Cicco et al., <https://doi.org/10.1088/1742-6596/190/1/012043>) by mounting the sample (as pellets) on a sample holder using Kapton tape in a vacuum chamber. The Si (1 1 1) fixed-exit double crystal monochromator of  $1.4 \times 10^{-4}$  resolving power was calibrated to the first-derivative maximum of the K-edge absorption spectrum of a metallic Fe foil (7112.0 eV) and it was detuned to exclude higher order harmonics.

## 2.4. Electrochemical Measurements

Typically, the electrochemical performance was measured using a Biologic electrochemical workstation instrument with techniques like Linear scanning voltammetry (LSV), cyclic voltammetry (CV), chronopotentiometry (CP), and Electrochemical impedance spectroscopy (EIS). All the electrochemical experiments were carried out in a three-electrode set-up (Ag/AgCl-reference, Pt wire-counter, and as-prepared catalysts-working electrode, electrolyte- 1.0 M KOH). Before measuring LSV, CV was performed at a scan rate of 50 mV s $^{-1}$  for 20 cycles to activate the surface of the catalyst. Then, LSV was carried out at a scan rate of 1 mV s $^{-1}$ . The electrochemical double-layer capacitance ( $C_{dl}$ ) of various electrocatalysts was also obtained using the CV in the non-Faradic area at varied sweeping speeds spanning from 180 mV s $^{-1}$  to 260 mV s $^{-1}$ . Electrochemical impedance spectroscopy (EIS) measurements were carried out from 0.1 to 100 000 Hz with an amplitude of 5 mV and an overpotential of 0.3 V. The electrochemical double-layer capacitance, expected to be linearly proportional to the Electrochemical active surface area (ECSA), was determined by measuring the capacitive current at non-Faradic regions from scan rate-dependent CV runs.

## 3. Results and Discussion

### 3.1. Theoretical Insights

The DFT calculations predicted the potential substitution sites for Ru in the Fe-Ti-O system. Ru could either replace Ti, forming Fe $_{2-x}$ Ru $_x$ TiO $_5$ , or Fe, resulting in Fe $_{2-x}$ Ru $_x$ TiO $_5$ . To resolve this ambiguity, the formation energies for both scenarios were calculated. Figure 1 presents the calculated formation energies for Fe $_2$ Ru $_x$ Ti $_{1-x}$ O $_5$  and Fe $_{2-x}$ Ru $_x$ TiO $_5$ . The results indicate that the formation of Fe $_{2-x}$ Ru $_x$ TiO $_5$  is slightly more thermodynamically favorable than that of Fe $_2$ Ru $_x$ Ti $_{1-x}$ O $_5$ , suggesting that Fe $_{2-x}$ Ru $_x$ TiO $_5$  may be the dominant phase in the real catalyst. However, the possible existence of Fe $_2$ Ru $_x$ Ti $_{1-x}$ O $_5$  cannot be excluded, prompting us to investigate the activity of both models toward the OER and UOR to better understand the active sites. Inspired by this, we experimentally produced the predicted systems.

### 3.2. Morphology, and Crystal Structure Characterizations

The pure Fe $_2$ TiO $_5$  pseudobrookite crystal phase with an orthorhombic space group, Bbmm (63), was achieved at 800 °C for 3 h and characterized by XRD. As depicted in Figure 2a, the diffraction reflections appeared at 18.1°, 25.5°, 32.4°, 36.5°, 37.4°, 45.9°, 48.7°, and 59.8°, corresponding to the (200), (101), (230), (301), (131), (430), (020), and (232) planes of Fe $_2$ TiO $_5$ . All peaks in the diffraction pattern agree with the standard PDF #41-1432, confirming the formation of the pure Fe $_2$ TiO $_5$  phase. To introduce Ru doping, different amounts of Ru precursor (0.04, 0.06, 0.08, and 1.0g) were considered to optimize the appropriate Ru content that could be incorporated without inducing an additional crystal phase in Fe $_2$ TiO $_5$ , aiming for the formation of Fe $_{2-x}$ Ru $_x$ TiO $_5$ . This was synthesized using hydrothermal synthesis followed by CVD treatment. The pure Fe $_{2-x}$ Ru $_x$ TiO $_5$  phase was achieved at x = 0.04 Ru content. XRD characterization (Figure 2a) of the Ru-doped material revealed reflection peaks like Fe $_2$ TiO $_5$ , with a slight shift of the (101) diffraction peak to a lower angle. This shift indicates an increase in interplanar spacing, suggesting the successful incorporation of Ru $^{4+}$  ions into the Fe $_2$ TiO $_5$  structure. However, as shown in Figure S1a (Supporting Information), when x exceeds 0.04, Ru tends to aggregate and form RuO $_2$  instead of incorporating into the Fe $_2$ TiO $_5$  lattice. This leads to the formation of a RuO $_2$ -Fe $_2$ TiO $_5$  heterostructure rather than true Ru doping. As illustrated in Figure 2b, the TEM analysis reveals that Fe $_2$ TiO $_5$  consists of nanoparticles, with a mean particle size of  $\approx$ 52 nm, as estimated from Figure S1b (Supporting Information) and further supported by Figure S1c (Supporting Information). The HRTEM images (Figure 2c) display that the nanoparticles are highly crystalline: crystal lattice spacing is observed and the corresponding SAED pattern (Figure 2d) shows a clear diffraction pattern. The marked crystal lattice spacing is 4.56, and 3.34 Å, corresponding to (111) and (220) crystallographic planes of Fe $_2$ TiO $_5$  (PDF #41-1432), which is consistent with XRD analysis and the standard patterns of Fe $_2$ TiO $_5$  (PDF #41-1432). When Ru was incorporated, the TEM image (Figure 2e) demonstrated that smaller particles (less than  $\approx$ 49 nm, Figure S1c, Supporting Information) could be observed on Fe $_{2-x}$ Ru $_x$ TiO $_5$ . With Ru loading, the HRTEM image (Figure 2f) and SAED pattern (Figure 2g) display diffraction spots at 2.88, 4.94, and 3.43 Å, corresponding to (121), (200), and (101) crystallographic planes of Ru doped Fe $_2$ TiO $_5$  structure, respectively. HAADF-STEM images (Figure 2h) and corresponding elemental mapping confirm the presence and spatially homogeneous distribution of Ru, Fe, Ti, and O elements uniformly dispersed in the Fe $_{2-x}$ Ru $_x$ TiO $_5$ .

XPS analysis was used to understand the samples' surface chemistry and oxidation states. Figure S2a,b (Supporting Information) shows the survey XPS spectra for Fe $_2$ TiO $_5$  and Fe $_{2-x}$ Ru $_x$ TiO $_5$  samples, which affirm the presence of all the expected elements, that is, Ti, Fe, O for Fe $_2$ TiO $_5$ , and the addition of Ru in the Fe $_{2-x}$ Ru $_x$ TiO $_5$ . The deconvoluted high-resolution Fe 2p core level spectrum of Fe $_2$ TiO $_5$  (Figure 3a), shows contributions at 724.1 and 710.8 eV assigned to the doublet Fe 2p $_{1/2}$  and Fe 2p $_{3/2}$ , respectively, indicating Fe $^{3+}$  with a 13.3 eV gap. Deconvolution revealed a contribution at 713.4 eV, and satellite peaks at 719.1 and 732.7 eV that confirm the oxidation state of Fe $^{3+}$ . In the Fe $_{2-x}$ Ru $_x$ TiO $_5$  sample, the high-resolution Fe 2p core level spectrum showed a slight shift of 0.2 eV toward lower binding

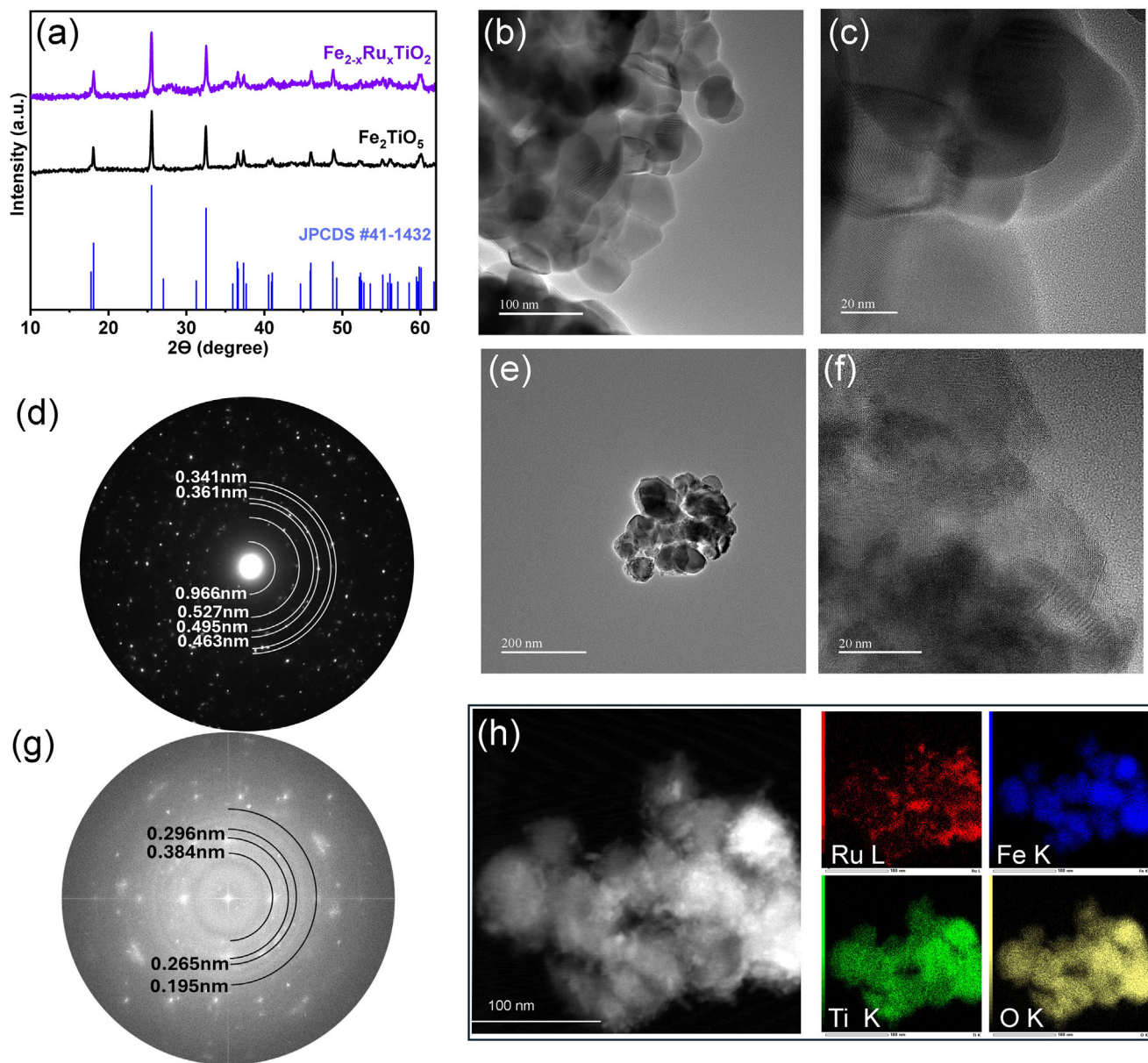


**Figure 2.** a) XRD, b) TEM image, c) HRTEM image d), SAED pattern of  $\text{Fe}_2\text{TiO}_5$ , e) TEM image, f) HRTEM image, g) SAED pattern of  $\text{Fe}_{2-x}\text{Ru}_x\text{TiO}_5$ , h) HAADF-STEM and corresponding elemental mapping of Ru, Fe, Ti, and O in  $\text{Fe}_{2-x}\text{Ru}_x\text{TiO}_5$ .

energies, suggesting a possible electron density redistribution between Ru and Fe at the surface region.

The BE of Ti  $2p$  in  $\text{Fe}_2\text{TiO}_5$  appeared at  $\approx 458.3$  and  $463.9$  eV, indicative of  $\text{Ti}^{4+}$  oxidation states, as shown in Figure 3b. Upon Ru doping, the Ti  $2p_{3/2}$  binding energy shifts to a higher energy of  $458.7$  eV, specifically by  $0.4$  eV, pointing out the electron density redistribution between Ru and Fe at the surface region. However, part of the doublet Ti  $2p_{1/2}$  is masked by the Ru  $3p_{3/2}$  signal. To further validate the oxidation state of Ti, we examined the Ti  $3p$  spectrum (Figure S2c, Supporting Information), which confirmed the presence of Ti (IV) ions, octahedrally coordinated by oxygen ions. As depicted in Figure 3c the Ru  $3d$  peaks at  $282.1$  eV and  $286.0$  eV confirmed the presence of  $\text{Ru}^{4+}$ . Due to the

Ru  $3d$  signal overlapping with the C  $1s$  signal, the Ru  $3p_{1/2}$  at  $488.1$  eV (Figure S2d, Supporting Information) was measured, further confirming the presence of  $\text{Ru}^{4+}$  in  $\text{Fe}_{2-x}\text{Ru}_x\text{TiO}_5$ . However, peaks at  $484.7$  and  $280.5$  eV in both Ru  $3p$  and Ru  $3d$  spectra indicated the presence of unreacted Ru (0) on the surface. Finally, the high-resolution O  $1s$  core level spectra (Figure S2e, Supporting Information) were resolved into two contributions: one at  $529.9$  eV, associated with lattice oxygen, and another  $\approx 531.4$  eV, attributed to Fe-OH groups in both doped and undoped samples. Hence, the combined study shows that the nano-structured material and Ru doping were successfully synthesized. To further explore the electronic structure and crystal structure distortion, Fe K-edge XAS spectra (Figure 3e) were collected for both

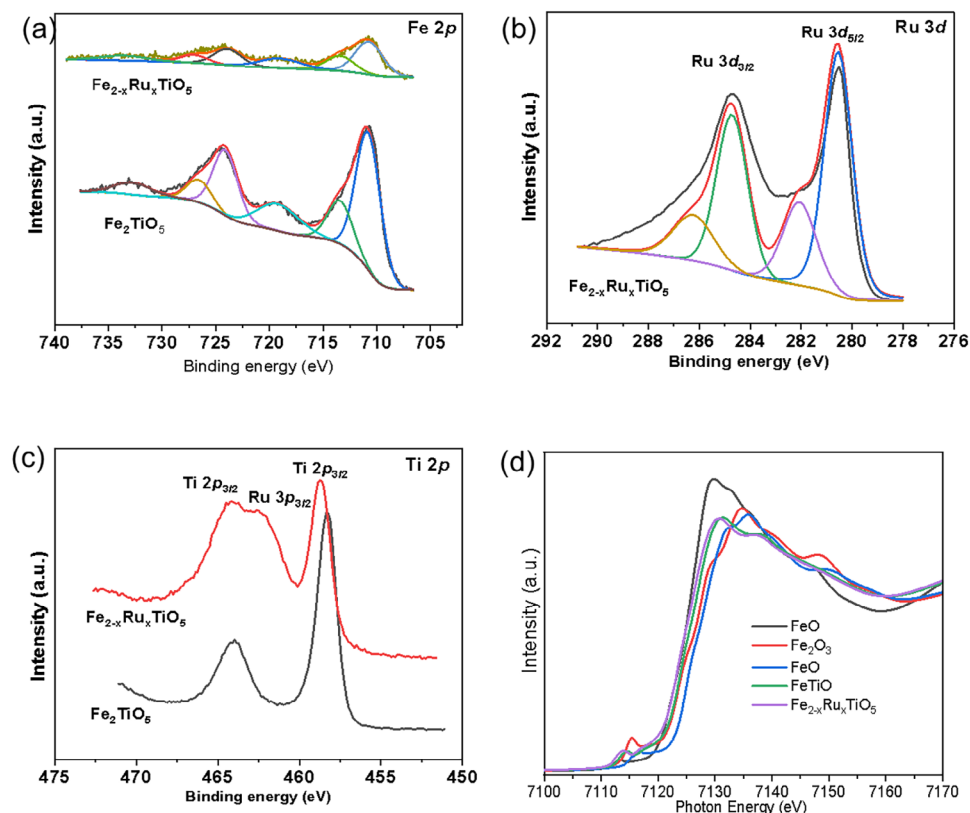


**Figure 3.** High-resolution XPS spectra of  $\text{Fe}_2\text{TiO}_5$  and  $\text{Fe}_{2-x}\text{Ru}_x\text{TiO}_5$ : a) Fe 2p b) Ti 2p c) Ru 3d and d) O 1s. e) XAS Fe K-edge spectra for FeO,  $\text{Fe}_2\text{O}_3$ ,  $\text{Fe}_3\text{O}_4$ ,  $\text{Fe}_2\text{TiO}_5$  and  $\text{Fe}_{2-x}\text{Ru}_x\text{TiO}_5$ .

$\text{Fe}_2\text{TiO}_5$  and  $\text{Fe}_{2-x}\text{Ru}_x\text{TiO}_5$  and compared with reference spectra from FeO,  $\text{Fe}_2\text{O}_3$ , and  $\text{Fe}_3\text{O}_4$ . The alignment of the Fe K-edge spectrum of  $\text{Fe}_2\text{TiO}_5$  with that of  $\text{Fe}_2\text{O}_3$  confirms the presence of  $\text{Fe}^{3+}$ . However, after Ru doping, the main edge shifts to lower photon energy, aligning with FeO, which indicates a partial reduction of Fe in  $\text{Fe}_{2-x}\text{Ru}_x\text{TiO}_5$  toward the  $\text{Fe}^{2+}$  state. This observation is consistent with our Fe 2p XPS results. Additionally, the change in pre-edge peak intensity in the Fe K-edge indicates a local structure distortion at the Fe site, further supported by our DFT calculations. This suggests that Ru substitutes the Fe site to form  $\text{Fe}_{2-x}\text{Ru}_x\text{TiO}_5$ . Our findings align closely with the results reported in earlier research studies.<sup>[53,54]</sup> This consistency suggests that our outcomes support the validity of the conclusions drawn by prior investigators.

### 3.3. Electrochemical Evaluation of UOR

The electrocatalytic performance of the designed samples for UOR was investigated using a standard three-electrode cell in a 1.0 M KOH solution with 0.5 M urea. **Figure 4a** shows the OER electrocatalytic performance of  $\text{Fe}_{2-x}\text{Ru}_x\text{TiO}_5$  and  $\text{Fe}_2\text{TiO}_5$ . Specifically, in 1 M KOH the potential required by Ni foam,  $\text{Fe}_2\text{TiO}_5$ , and  $\text{Fe}_{2-x}\text{Ru}_x\text{TiO}_5$  for OER to reach a current density of  $10 \text{ mA cm}^{-2}$  is 1.75, 1.61 and 1.50 V. However, with 1 M KOH + 0.5 M urea, the potential at  $100 \text{ mA cm}^{-2}$  ( $E_{100}$ ) of this catalyst can reach 1.6 V,  $\approx 140 \text{ mV}$  lower than that in the pure KOH so-

lution, implying that the UOR is more energy-efficient than the OER for  $\text{Fe}_{2-x}\text{Ru}_x\text{TiO}_5$ . The  $\text{Fe}_2\text{TiO}_5$  catalyst requires potentials of 1.61, 1.70, and 1.80 V to achieve current densities of 10, 50, and  $100 \text{ mA cm}^{-2}$  for the OER (Figure S4a, Supporting Information). However, after Ru doping,  $\text{Fe}_{2-x}\text{Ru}_x\text{TiO}_5$  shows a significant reduction in the required potentials, needing only 1.50, 1.62, and 1.74 V for the same current densities. A similar trend is observed under UOR conditions (Figure 4c), where  $\text{Fe}_{2-x}\text{Ru}_x\text{TiO}_5$  achieves 10, 50, and  $100 \text{ mA cm}^{-2}$  at 1.29, 1.50, and 1.60 V, respectively, in contrast to  $\text{Fe}_2\text{TiO}_5$ , which requires 1.55, 1.71, and 1.80 V. The significant change in potential in Ru doped sample and under the presence of Urea reflects that Ru doping and urea play a crucial role in enhancing catalytic performance. For a fairer comparison that would eliminate the influence of the catalyst's surface area and focus on its true intrinsic activity, we normalized the data with ECSA.<sup>[55]</sup> As can be seen from Figure S4b (Supporting Information), a similar trend is observed which illustrates that electrocatalytic performance emanates from the intrinsic behavior.

To better understand the UOR and OER kinetics, the Tafel slopes for doped and undoped samples were determined. As a result,  $\text{Fe}_{2-x}\text{Ru}_x\text{TiO}_5$  displays a remarkably smaller Tafel slope of  $52 \text{ mV dec}^{-1}$  in UOR (Figure 4d) compared to the Tafel plot of  $92 \text{ mV dec}^{-1}$  in OER (Figure 4e), indicating a rapid current density increase and favorable kinetics for UOR. The performance and kinetics of  $\text{Fe}_{2-x}\text{Ru}_x\text{TiO}_5$  for UOR were also compared with literature reports, demonstrating superior activity and fast kinetics surpassing the most recently reported works, as shown in

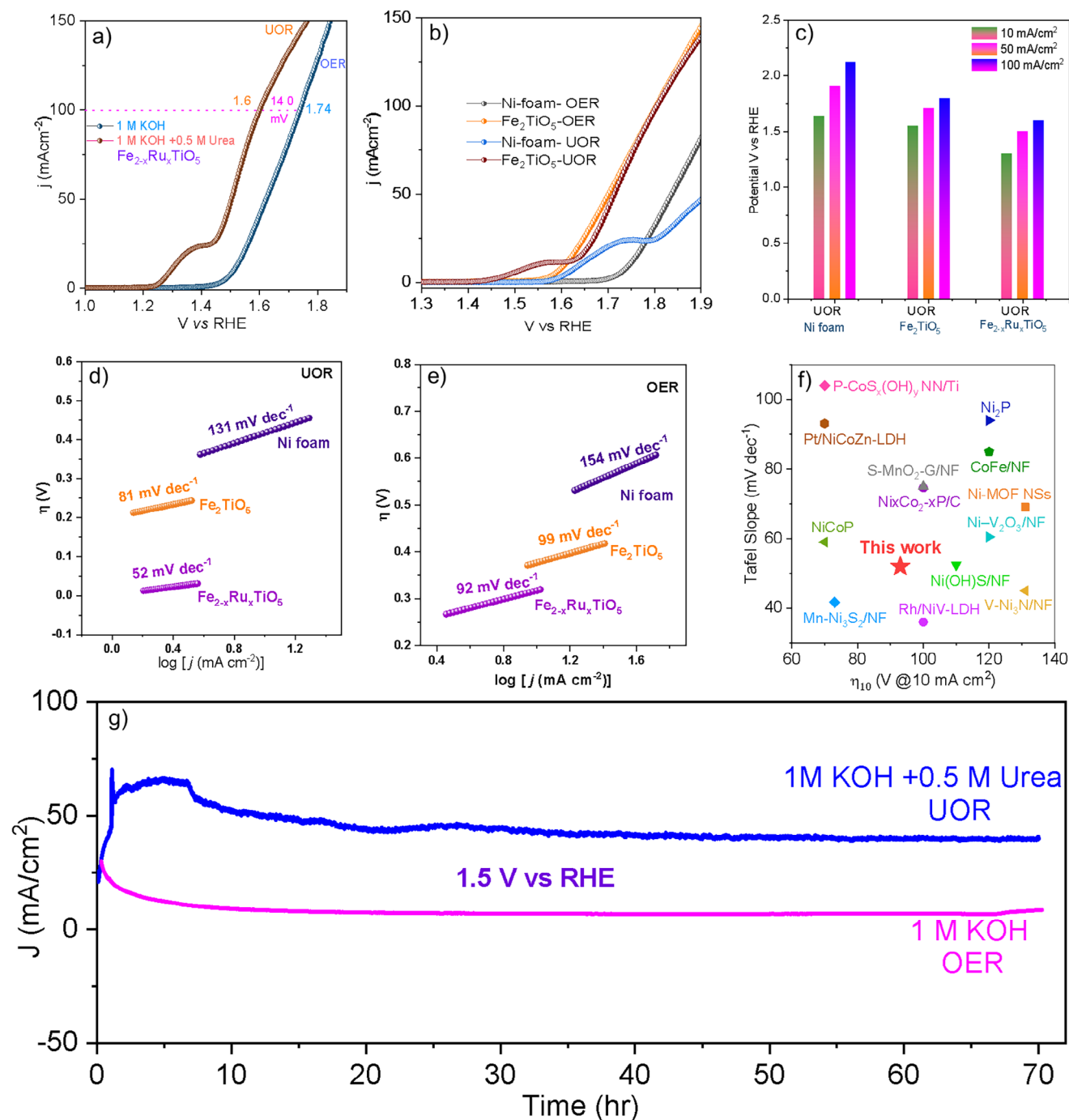


**Figure 4.** a) Polarization curves of  $\text{Fe}_{2-x}\text{Ru}_x\text{TiO}_5$  electrocatalysts in 1.0 M KOH with and without 0.5 M urea. b) LSV curves of NF and  $\text{Fe}_2\text{TiO}_5$ . c) Comparison of UOR potentials at 10, 50, and 100 mA cm<sup>-2</sup> current densities. Tafel plots for d) UOR and e) OER. f) Comparison of the UOR overpotential of  $\text{Fe}_{2-x}\text{Ru}_x\text{TiO}_5$  at a current density of 10 mA cm<sup>-2</sup> with other reported works. g) Chronoamperometric run of  $\text{Fe}_{2-x}\text{Ru}_x\text{TiO}_5$  for the long-term durability test at 1.5 V.

Figure 4f. To investigate the reasons for the high UOR activity of  $\text{Fe}_{2-x}\text{Ru}_x\text{TiO}_5$ , we first calculated its double-layer capacitance ( $C_{dl}$ ), which is proportional to the electrochemical active surface area (ECSA). To unveil this, we calculated the  $C_{dl}$  by monitoring the current density in the non-Faradic region with different scan rates. The CV run for obtaining these data is pre-

sented in Figure S3c–f (Supporting Information). As a result, Figure S4a,b (Supporting Information) shows the  $C_{dl}$  value of  $\text{Fe}_2\text{TiO}_5$  (27.7 mF cm<sup>-2</sup>, UOR and 30.0 mF cm<sup>-2</sup>, OER) and  $\text{Fe}_{2-x}\text{Ru}_x\text{TiO}_5$  (33.0 mF cm<sup>-2</sup>, UOR and 35.8 mF cm<sup>-2</sup>, OER), respectively. The UOR  $C_{dl}$  value for Ru doping of  $\text{Fe}_{2-x}\text{Ru}_x\text{TiO}_5$  is 2.7 times higher than that of  $\text{Fe}_2\text{TiO}_5$ , demonstrating that Ru

doping can greatly improve the UOR intrinsic activity. Moreover, the EIS at the solid–liquid interface was measured to study electrical conductivity. As shown in Figure S4c (Supporting Information),  $\text{Fe}_{2-x}\text{Ru}_x\text{TiO}_5$  exhibits a charge transfer resistance ( $R_{ct}$ ) of only  $0.91\ \Omega$ , lower than  $\text{Fe}_2\text{TiO}_5$  ( $1.02\ \Omega$ ) under UOR. Similarly, under OER,  $\text{Fe}_{2-x}\text{Ru}_x\text{TiO}_5$  shows an  $R_{ct}$  (Figure S4d, Supporting Information) of only  $1.75\ \Omega$ , again lower than that of  $\text{Fe}_2\text{TiO}_5$  ( $1.78\ \Omega$ ), implying the enhanced electron transfer rate in  $\text{Fe}_{2-x}\text{Ru}_x\text{TiO}_5$ .

In addition to catalytic activity, stability is another fundamental criterion for evaluating catalysts. Herein, we examined the Chronoamperometric performance (Figure 4g) of the catalyst at a potential of 1.5 V over an extended period of 72 hr with negligible potential change, signifying the robust OER and UOR stability. We also examined the Chronopotentiometric performance (Figure S4e, Supporting Information) at fixed current densities ( $10$ ,  $50$ , and  $150\ \text{mA cm}^{-2}$ ) over an extended period of 36 hr. At lower current densities of  $10$  and  $50\ \text{mA cm}^{-2}$ , the catalyst exhibited stable potentials for both OER and UOR. However, at a higher current density of  $150\ \text{mA cm}^{-2}$ , a slight drop in potential was observed only in OER, with no corresponding change observed in the UOR counterpart. It is noteworthy that the increase in potential during OER occurred primarily in the final hours, while the potential remained relatively constant during the initial hours. The long-term stability for  $\text{Fe}_{2-x}\text{Ru}_x\text{TiO}_5$  under KOH and KOH + urea also compares fairly with the most recently reported literature, as displayed in Table S1 (Supporting Information). This impressive resilience suggests the potential for long-term practical applications of the catalysts.

Meanwhile, after drop-casting  $\text{Fe}_{2-x}\text{Ru}_x\text{TiO}_5$  onto Ni foam, post-UOR XRD analysis was conducted to evaluate the catalyst's structural stability. Although the intense peaks from the Ni foam obscure some characteristic peaks of our material, an enlarged peak (Figure S5, Supporting Information) is still observed at  $25.5^\circ$  and  $32.4^\circ$ , corresponding to the (101) and (230) planes of  $\text{Fe}_{2-x}\text{Ru}_x\text{TiO}_5$ . This confirms the material's stability even after long-term operation.

### 3.4. Mechanism of Electrocatalytic Urea Oxidation Reaction

Experimental efforts unveiled that the rationally synthesized  $\text{Fe}_{2-x}\text{Ru}_x\text{TiO}_5$  holds superior catalytic activity and robust stability. To further understand the reaction mechanism and the underlying reason for the higher activity, density functional theory (DFT) simulations were conducted. Given the nature of the catalyst surface, we proposed two possible mechanisms to investigate the OER reaction: the adsorbate evolution mechanism (AEM), based on the evolution of adsorbed intermediates, and the lattice oxygen mechanism (LOM), where lattice oxygen could be involved in the OER process, as depicted in Figure 5a. Similarly, Figure 5b presents the OER energy profile for the three models using the AEM mechanism. The data show that the  $\text{Fe}_2\text{TiO}_5$  catalyst has a high energy barrier of 2.25 eV, with a potential-limiting step of 1.02 V. This suggests that OER processing on the  $\text{Fe}_2\text{TiO}_5$  surface is challenging at low electrode potentials, with the rate-determining step being the transformation of  $^*\text{OH}$  to  $^*\text{O}$ . The introduction of a Ru atom in place of Ti reduces the barrier energy to 1.94 eV, and the potential-determining step decreases to

0.71 V, still associated with the  $^*\text{OH}$  to  $^*\text{O}$  transformation. A similar activity is observed when Ru substitutes for Fe, with a barrier energy of  $\approx 1.97$  eV and an overpotential of  $\approx 0.74$  V. In all three models, the rate-determining step is the  $^*\text{OH}$  to  $^*\text{O}$  transformation, which can be attributed to the high oxidation environment of the  $\text{Fe}_2\text{TiO}_5$  catalyst and its Ru-doped counterpart. This high oxidation environment necessitates a significant energy barrier for the formation of the  $^*\text{O}$  intermediate, which is moderated by the introduction of Ru atoms at the Ti or Fe sites.

Due to the high oxidation environment of the catalyst models, we also investigated the LOM mechanism, exploring the possibility of lattice oxygen involvement in  $\text{O}_2$  production via association with the  $^*\text{O}$  intermediate. The energy profile depicted in Figure 5c shows that the associative process of the  $^*\text{O}$  intermediate with lattice oxygen to form  $\text{O}_2$  and create an oxygen vacancy requires high barrier energies. These barriers are  $\approx 1.70$ , 2.55, and 1.42 eV for the  $\text{Fe}_2\text{TiO}_5$ ,  $\text{Fe}_2\text{Ru}_x\text{Ti}_{1-x}\text{O}_5$ , and  $\text{Fe}_{2-x}\text{Ru}_x\text{TiO}_5$  catalyst models, respectively, indicating a significant likelihood of occurrence under real operating conditions.

We next examine the UOR mechanism in the three models, beginning with an analysis of the urea adsorption energy as an initial step for subsequent oxidation. As illustrated in Figure 5d, urea exhibits the highest adsorption energy of  $\approx -1.01$  eV on the  $\text{Fe}_2\text{Ru}_x\text{Ti}_{1-x}\text{O}_5$  surface, while the  $\text{Fe}_{2-x}\text{Ru}_x\text{TiO}_5$  surface shows a moderate adsorption energy of  $\approx -0.81$  eV. In contrast, the pristine  $\text{Fe}_2\text{TiO}_5$  surface demonstrates a relatively low adsorption energy of  $\approx -0.43$  eV. The subsequent reaction pathway, detailed in Figure 5e, reveals that all three models adsorb urea more strongly than the  $^*\text{OH}$  intermediate. This suggests that, under operational conditions, urea can preferentially occupy the catalyst's active sites due to its higher adsorption energy compared to  $\text{OH}^-$ .

The initial step of urea activation is critical, as it determines the feasibility of urea decomposition. As shown in Figure 5e, the first step of urea dehydrogenation requires a barrier energy of 1.76 eV on the pristine  $\text{Fe}_2\text{TiO}_5$  surface. In contrast, this barrier is significantly lower in the Ru-doped models, requiring 1.12 eV on  $\text{Fe}_2\text{Ru}_x\text{Ti}_{1-x}\text{O}_5$  and 1.26 eV on  $\text{Fe}_{2-x}\text{Ru}_x\text{TiO}_5$ . Notably, this first step is the rate-determining step for the pristine  $\text{Fe}_2\text{TiO}_5$  surface, but not for the doped models. For  $\text{Fe}_2\text{Ru}_x\text{Ti}_{1-x}\text{O}_5$ , the rate-determining step is the third dehydrogenation step, with a barrier energy of 1.29 eV. For  $\text{Fe}_{2-x}\text{Ru}_x\text{TiO}_5$ , the second dehydrogenation step is rate-limiting, with a barrier energy of 1.62 eV. These findings suggest that high adsorption of certain reaction intermediates and control of their adsorption energy and interactions with the catalyst surface can enhance urea oxidation.

To better understand the effect of Ru doping on the Fe active site in  $\text{Fe}_2\text{TiO}_5$ , we performed a projected density of states (PDOS) analysis, as shown in Figure 6a,b. The results indicate that the introduction of Ru atoms shifts the Fe 3d orbitals upward, suggesting a reduction in the oxidation state of the Fe sites. This shift helps to explain the enhanced adsorption of reactants, including the OH intermediate for the OER reaction and urea. Notably, we also observed a splitting of the Fe 3d orbitals, with the  $dz^2$  and  $dxz$  orbitals shifting to higher energy levels. These results may also indicate a crystal structure distortion, consistent with observations from experimental results from the XPS Fe 2p spectra (Figure 3a) and Fe K-edge XAS (Figure 3e).

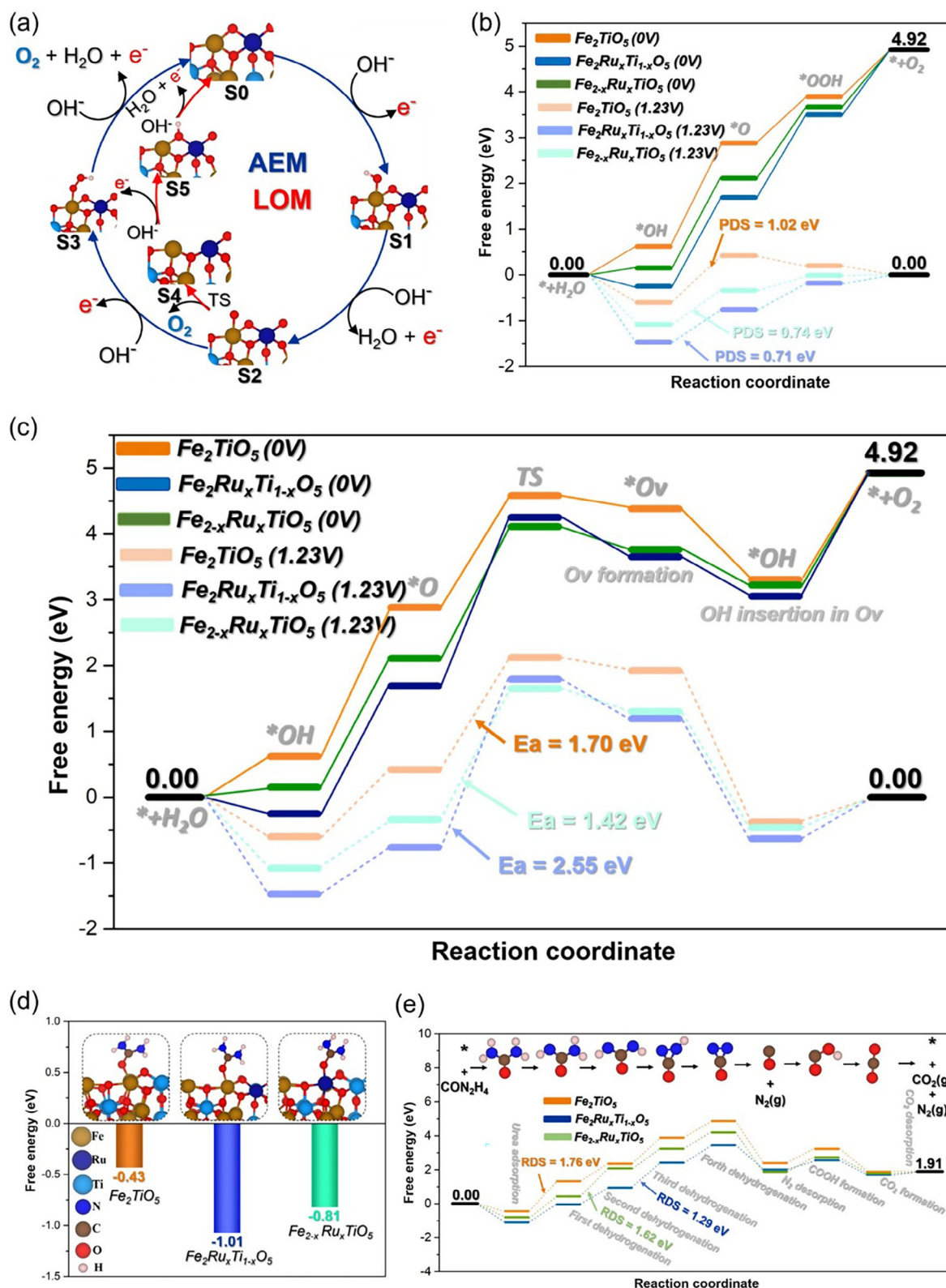


**Figure 5.** a) OER mechanism pathways via AEM and LOM on  $\text{Fe}_2\text{Ru}_x\text{Ti}_{1-x}\text{O}_5$ . b) OER energy profile on  $\text{Fe}_2\text{TiO}_5$ ,  $\text{Fe}_2\text{Ru}_x\text{Ti}_{1-x}\text{O}_5$ , and  $\text{Fe}_{2-x}\text{Ru}_x\text{TiO}_5$  via AEM mechanism calculated at 0 V and 1.23 V. c) OER energy profile on  $\text{Fe}_2\text{TiO}_5$ ,  $\text{Fe}_2\text{Ru}_x\text{Ti}_{1-x}\text{O}_5$ , and  $\text{Fe}_{2-x}\text{Ru}_x\text{TiO}_5$  via LOM mechanism calculated at 0 and 1.23 V. d) Urea adsorption energy on different catalyst models  $\text{Fe}_2\text{TiO}_5$ ,  $\text{Fe}_2\text{Ru}_x\text{Ti}_{1-x}\text{O}_5$  and  $\text{Fe}_{2-x}\text{Ru}_x\text{TiO}_5$ . e) Urea oxidation energy profile on  $\text{Fe}_2\text{TiO}_5$ ,  $\text{Fe}_2\text{Ru}_x\text{Ti}_{1-x}\text{O}_5$ , and  $\text{Fe}_{2-x}\text{Ru}_x\text{TiO}_5$ .

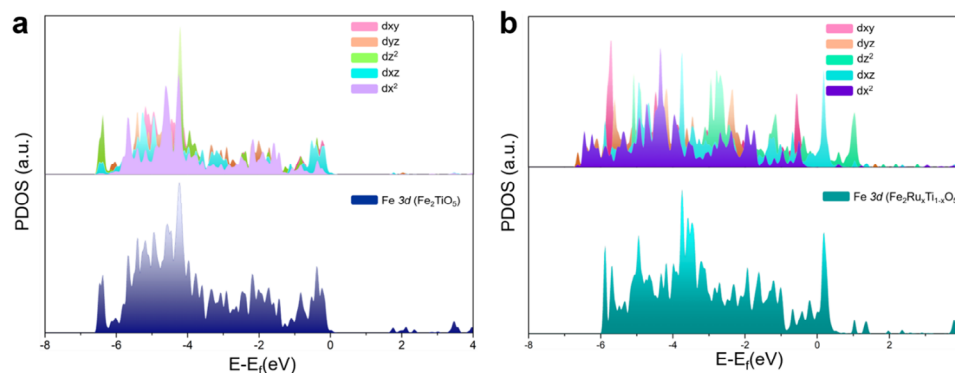


**Figure 6.** Partial density of states (PDOS) of d-projected DOS of Fe active site in a)  $\text{Fe}_2\text{TiO}_5$  and b)  $\text{Fe}_2\text{Ru}_x\text{Ti}_{1-x}\text{O}_5$ .

## 4. Conclusion

In summary, Ru-doped pseudobrookite  $\text{Fe}_2\text{TiO}_5$  was successfully synthesized using a two-step hydrothermal treatment. This approach yielded a sample with high crystallinity, well-defined morphology, and precise ruthenium doping, as predicted by first-principles calculations. Additionally, the resulting nanostructure demonstrated exceptional efficiency and stability as an electrocatalyst for both OER and UOR. Its low overpotential of 150 mV, a Tafel slope of  $52 \text{ mV dec}^{-1}$ , and remarkable stability over 72 h make this material one of the most promising candidates in the UOR field. From the DFT simulation, Ru-doped models showed higher urea adsorption energies and lower energy barriers for initial dehydrogenation steps to the pristine  $\text{Fe}_2\text{TiO}_5$ . The Ru doping donates electrons back at large overpotential and prevents Fe dissolution, as confirmed via first-principle computation. The dynamic electron interaction between Ru and Fe facilitates the adsorbate evolution mechanism and lowers adsorption energies for oxygen intermediates to boost the activity and stability of  $\text{Fe}_2\text{Ru}_x\text{Ti}_{1-x}\text{O}_5$ . This study paves the way for advancing water oxidation through innovative material development and using urea-assisted water splitting, which collectively helps oxidation reduce water oxidation's kinetics.

## Supporting Information

Supporting Information is available from the Wiley Online Library or from the author.

## Acknowledgements

This work was partially supported by the Kempe Foundation, the Knut och Alice Wallenberg Foundation (grant number KAW 2016.346), the ÅFORSK Foundation, the European Union – NextGenerationEU, in the framework of the iNEST – Interconnected Nord-Est Innovation Ecosystem (iNEST ECS\_00000043 – CUP H43C22000540006) and NEST – Network4 Energy Sustainable Transition (PE0000021 – CUP D43C22003090001). The authors would also like to acknowledge Ca' Foscari University of Venice for the SPIN2019 project, Elettra Sincrotrone Trieste for providing access to its synchrotron radiation facilities. Finally, T.A. Shifa acknowledges the MSCA-IF-2020, CoCaWS, 101027930 and PRIN 2022, CUP: H53D23003840001 and K.B. Ibrahim acknowledges the PNRR RTD A. E.R.C. thanks Ministerio de Ciencia e Innovación, Spain (Grant TED2021-130756B-C31 MCIN/AEI/10.13039/501100011033) and “ERDF A way of making Europe” by the European Union NextGenerationEU/PRTR.

Open access publishing facilitated by Università Ca' Foscari, as part of the Wiley - CRUI-CARE agreement.

## Conflict of Interest

The authors declare no conflict of interest.

## Author Contributions

K.B.I., M.H., K.H., and M.B. contributed equally to this work. A.V., K.B.I., and E.M. supervised the project. T.A.S. conceived and designed the project. P.S. and M.H. perform the ECSA and EIS measurements. K.H. carried out the theoretical calculation. S.B., D.H. TEM characterization and E. R-C: XPS characterization assisted in material characterizations. D.O.D.-S., and L.O. measure XAS, M.G.S., and M.B. wrote the manuscript in consultation with all the other authors.

## Data Availability Statement

The data that support the findings of this study are available from the corresponding author upon reasonable request.

## Keywords

$\text{Fe}_{2-x}\text{Ru}_x\text{TiO}_5$ , Oxygen Evolution reaction, pseudobrookite, urea-assisted water oxidation, Urea Oxidation reaction

Received: December 18, 2024  
Revised: February 4, 2025  
Published online: March 10, 2025

- [1] Z. Ji, J. Liu, Y. Deng, S. Zhang, Z. Zhang, P. Du, Y. Zhao, X. Lu, *J. Mater. Chem. A* **2020**, *8*, 14680.
- [2] J. Liang, Z. Cai, Z. Li, Y. Yao, Y. Luo, S. Sun, D. Zheng, Q. Liu, X. Sun, B. Tang, *Nat. Commun.* **2024**, *15*, 2950.
- [3] T. A. Shifa, A. Gradone, K. Yusupov, K. B. Ibrahim, M. Jugovac, P. M. Sheverdyayeva, J. Rosen, V. Morandi, P. Moras, A. Vomiero, *Chem. Eng. J.* **2023**, *453*, 139781.
- [4] B. Zhao, J. Liu, C. Xu, R. Feng, P. Sui, J.-X. Luo, L. Wang, J. Zhang, J.-L. Luo, X.-Z. Fu, *Appl. Catal., B* **2021**, *285*, 119800.
- [5] X. Deng, M. Li, Y. Fan, L. Wang, X.-Z. Fu, J.-L. Luo, *Appl. Catal., B* **2020**, *278*, 119339.

- [6] S. Hu, S. Wang, C. Feng, H. Wu, J. Zhang, H. Mei, *ACS Sustainable Chem. Eng.* **2020**, *8*, 7414.
- [7] S. Wang, L. Zhao, J. Li, X. Tian, X. Wu, L. Feng, *J. Energy Chem.* **2022**, *66*, 483.
- [8] Q. Qian, J. Zhang, J. Li, Y. Li, X. Jin, Y. Zhu, Y. Liu, Z. Li, A. El-Harairy, C. Xiao, G. Zhang, Y. Xie, *Angew. Chem., Int. Ed.* **2021**, *60*, 5984.
- [9] S. Liang, L. Pan, T. Thomas, B. Zhu, C. Chen, J. Zhang, H. Shen, J. Liu, M. Yang, *Chem. Eng. J.* **2021**, *415*, 128864.
- [10] C. Wei, Z. J. Xu, *Small Methods* **2018**, *2*, 1800168.
- [11] C. Li, Y. Liu, Z. Zhuo, H. Ju, D. Li, Y. Guo, X. Wu, H. Li, T. Zhai, *Adv. Energy Mater.* **2018**, *8*, 1801775.
- [12] X. Gu, D. Yang, Z. Liu, S. Wang, L. Feng, *Electrochim. Acta* **2020**, *353*, 136516.
- [13] A. S. Rasal, H. M. Chen, W.-Y. Yu, *Nano Energy* **2024**, *121*, 109183.
- [14] N. Chen, Y.-X. Du, G. Zhang, W.-T. Lu, F.-F. Cao, *Nano Energy* **2021**, *81*, 105605.
- [15] A. N. Rollinson, J. Jones, V. Dupont, M. V. Twigg, *Energy Environ. Sci.* **2011**, *4*, 1216.
- [16] J. Li, S. Wang, J. Chang, L. Feng, *Adv. Powder Mater.* **2022**, *1*, 100030.
- [17] J. Li, X. Xu, X. Hou, S. Zhang, G. Su, W. Tian, H. Wang, M. Huang, A. Toghan, *Nano Res.* **2023**, *16*, 8853.
- [18] J. Xie, R. Ding, Y. Li, J. Guo, Y. Zhang, Q. Fang, M. Yan, Y. He, Z. Yan, Z. Chen, X. Guo, Q. Yang, J. Luo, Y. Zhang, X. Sun, E. Liu, *Nano Energy* **2024**, *126*, 109669.
- [19] Y. Liu, D. Zheng, Y. Zhao, P. Shen, Y. Du, W. Xiao, Y. Du, Y. Fu, Z. Wu, L. Wang, *Int. J. Hydrogen Energy* **2022**, *47*, 25081.
- [20] T. Yu, Q. Xu, J. Chen, G. Qian, X. Zhuo, H. Yang, S. Yin, *Chem. Eng. J.* **2022**, *449*, 137791.
- [21] Y. Zhou, Y. Wang, D. Kong, Q. Zhao, L. Zhao, J. Zhang, X. Chen, Y. Li, Y. Xu, C. Meng, *Adv. Funct. Mater.* **2023**, *33*, 2210656.
- [22] J. Wang, Y. Sun, Y. Qi, C. Wang, *ACS Appl. Mater. Interfaces* **2021**, *13*, 57392.
- [23] M. Bollu, D. T. Tran, S. Prabhakaran, D. H. Kim, N. H. Kim, J. H. Lee, *Nano Energy* **2024**, *123*, 109413.
- [24] F. Luo, S. Pan, Y. Xie, C. Li, Y. Yu, Z. Yang, *J. Energy Chem.* **2024**, *90*, 1.
- [25] B. Zhu, Z. Liang, R. Zou, *Small* **2020**, *16*, 1906133.
- [26] F. O. Boakye, M. G. Sendeku, A. Kumar, S. Ajmal, K. A. Owusu, K. B. Ibrahim, M. Tabish, F. uz Zaman, M. A. Mushtaq, K. M. Alotaibi, *Appl. Catal. B: Environ. Energy* **2024**, *352*, 124013.
- [27] Y. Vlamidis, S. Forti, A. Rossi, C. Marinelli, C. Coletti, S. Heun, S. Veronesi, *Part. Part. Syst. Character.* **2024**, *41*, 2400141.
- [28] X. Zhang, Y. Ding, G. Wu, X. Du, *Int. J. Hydrogen Energy* **2020**, *45*, 30611.
- [29] Q. Gan, X. Cheng, J. Chen, D. Wang, B. Wang, J. Tian, T. T. Isimjan, X. Yang, *Electrochim. Acta* **2019**, *301*, 47.
- [30] K. B. Ibrahim, T. A. Shifa, M. Bordin, E. Moretti, H.-L. Wu, A. Vomiero, *Small Methods* **2023**, *7*, 2300348.
- [31] F. Li, J. Chen, D. Zhang, W.-F. Fu, Y. Chen, Z. Wen, X.-J. Lv, *Chem. Commun.* **2018**, *54*, 5181.
- [32] D. Xu, Z. Fu, D. Wang, Y. Lin, Y. Sun, D. Meng, T. feng Xie, *Phys. Chem. Chem. Phys.* **2015**, *17*, 23924.
- [33] H. Bandal, K. K. Reddy, A. Chaugule, H. Kim, *J. Power Sources* **2018**, *395*, 106.
- [34] K. Belay Ibrahim, T. Ahmed Shifa, S. Zorzi, M. Getaye Sendeku, E. Moretti, A. Vomiero, *Prog. Mater. Sci.* **2024**, *144*, 101287.
- [35] X. Wang, Z. Li, S. Sun, H. Sun, C. Yang, Z. Cai, H. Zhang, M. Yue, M. Zhang, H. Wang, *J. Colloid Interface Sci.* **2024**, *662*, 596.
- [36] W. Tang, J. Zou, Z. Li, X. Zhang, T. Xie, J. Li, X. He, X. Tang, X. Liu, W. Chu, *Catal. Sci. Technol.* **2024**, *14*, 2717.
- [37] K. B. Ibrahim, T. A. Shifa, P. Moras, E. Moretti, A. Vomiero, *Small* **2023**, *19*, 2204765.
- [38] S. Zou, M. S. Burke, M. G. Kast, J. Fan, N. Danilovic, S. W. Boettcher, *Chem. Mater.* **2015**, *27*, 8011.
- [39] Y. Gan, Y. Ye, X. Dai, X. Yin, Y. Cao, R. Cai, B. Feng, Q. Wang, X. Zhang, *Small* **2023**, *19*, 2303250.
- [40] L. Guo, J. Chi, J. Zhu, T. Cui, J. Lai, L. Wang, *Appl. Catal., B* **2023**, *320*, 121977.
- [41] M. G. Sendeku, T. A. Shifa, F. T. Dajan, K. B. Ibrahim, B. Wu, Y. Yang, E. Moretti, A. Vomiero, F. Wang, *Adv. Mater.* **2024**, *36*, 2308101.
- [42] Y. Tong, P. Chen, M. Zhang, T. Zhou, L. Zhang, W. Chu, C. Wu, Y. Xie, *ACS Catal.* **2018**, *8*, 1.
- [43] X. Gao, X. Bai, P. Wang, Y. Jiao, K. Davey, Y. Zheng, S.-Z. Qiao, *Nat. Commun.* **2023**, *14*, 5842.
- [44] A. J. Hensley, K. Ghale, C. Rieg, T. Dang, E. Anderst, F. Studt, C. T. Campbell, J.-S. McEwen, Y. Xu, *J. Phys. Chem. C* **2017**, *121*, 4937.
- [45] L. Li, Q. Sun, X. Liu, C. Wu, H. Zhao, C. Zhang, *Algorith. Architect. Parallel Proces.* **2018**, *18*, 15.
- [46] G. Kresse, D. Joubert, *Phys. Rev. B* **1999**, *59*, 1758.
- [47] P. E. Blöchl, *Phys. Rev. B* **1994**, *50*, 17953.
- [48] K. Harrath, Z. Yao, Y.-F. Jiang, Y.-G. Wang, J. Li, *J. Phys. Chem. C* **2024**, *128*, 5579.
- [49] K. Harrath, Z. Yao, Y.-F. Jiang, Y.-G. Wang, J. Li, *J. Phys. Chem. Lett.* **2023**, *14*, 4033.
- [50] L. Bahri, F. Mbarki, K. Harrath, *Chem. Pap.* **2023**, *77*, 3759.
- [51] S. Grimme, *Wiley Interdiscip. Rev.: Comput. Mol. Sci.* **2011**, *1*, 211.
- [52] I. C. Man, H. Y. Su, F. Calle-Vallejo, H. A. Hansen, J. I. Martínez, N. G. Inoglu, J. Kitchin, T. F. Jaramillo, J. K. Nørskov, J. Rossmeisl, *ChemCatChem* **2011**, *3*, 1159.
- [53] M.-C. Tsai, T.-T. Nguyen, N. G. Akalework, C.-J. Pan, J. Rick, Y.-F. Liao, W.-N. Su, B.-J. Hwang, *ACS Catal.* **2016**, *6*, 6551.
- [54] Y. Liu, Y. Ying, L. Fei, Y. Liu, Q. Hu, G. Zhang, S. Y. Pang, W. Lu, C. L. Mak, X. Luo, L. Zhou, M. Wei, H. Huang, *J. Am. Chem. Soc.* **2019**, *141*, 8136.
- [55] H. Ren, Y. Pan, C. C. Sorrell, H. Du, *J. Mater. Chem. A* **2020**, *8*, 3154.